REAL TIME, *IN-SITU* CURVATURE MEASUREMENTS OF EPITAXIAL YBCO FILMS ON MGO

D. Boyd, A. Tripathi, D. Owen, A. Rosakis, H. Atwater, and D. Goodwin
Divisions of Engineering and Applied Physics, California Institute of Technology,
Pasadena, CA 91125, daboyd@its.caltech.edu

ABSTRACT

We have implemented coherent gradient sensing (CGS) as an *in-situ* diagnostic in an MOCVD reactor to measure curvature and changes in curvature with varying temperature and O_2 partial pressure on thin film YBCO on MgO (001) substrates. CGS is a novel, real-time, full-field optical technique that provides a direct map of the components of the curvature tensor across the surface of the wafer. We have examined a well-characterized, YBCO film (700 nm thick) on a MgO substrate (25 x 25 x 0.5 mm) with increasing temperature from 25 °C to 760 °C The curvature increases with temperature, although it is not always spatially uniform. By Stoney's equation, we relate the observed curvature to the thermal mismatch of the film and substrate where the maximum observed stress in orthogonal sample orientations is 2.2 and 1.0 GPa. For larger similarly grown wafers under varying oxygen partial pressures, we observe dramatic local changes in the CGS interferograms, which we relate to the tetragonal to orthorhombic phase transformation YBCO exhibits as it cools in oxygen.

INTRODUCTION

Metal Organic Chemical Vapor Deposition (MOCVD) is a widely used thin film deposition process. With future demand for more complex layered materials, current open loop deposition recipes will not suffice, and real time sensing will be necessary for closed loop control. MOCVD processes present challenges for *in-situ* diagnostics; high background pressures and long working distances exclude even the most robust electron based diagnostics. Optical methods are preferable and typically have been used to obtain dielectric constants, film thickness, and in certain cases, spectroscopic information, however these methods are typically point wise, relative to the specimen, and therefore provide only a localized characterization. At best, these pointwise methods can scan the sample, at the expense of time, making it difficult to implement in a control-loop. Macroscopic properties such as curvature and relative coverage are problem areas, especially for production of larger diameter wafers. Full-field methods, where an entire specimen is imaged, are natural extensions of point-wise methods and offer increased throughput by providing instantaneous, relative spatial information. The relative nature of the measurement is attractive for processes for which uniformity is of concern and with appropriate image analysis methods may be suitable as a diagnostic.

Stress effects in thin film systems are of theoretical and practical interest, however, standard methods of measuring the related curvature tensor, $\boldsymbol{\kappa}$, are either difficult to apply *in-situ* and in real time (x-ray diffraction [1]), do not give an instantaneous full field map of the curvature tensor (beam bending [2]), or are sensitive to external vibrations (interferometric methods [3]). For control and industrial applications, robust techniques which can give a clear indication on the curvature state of the film are desirable for diagnostics.

Based on beam shearing methods, Coherent Gradient Sensing is a full-field, real time

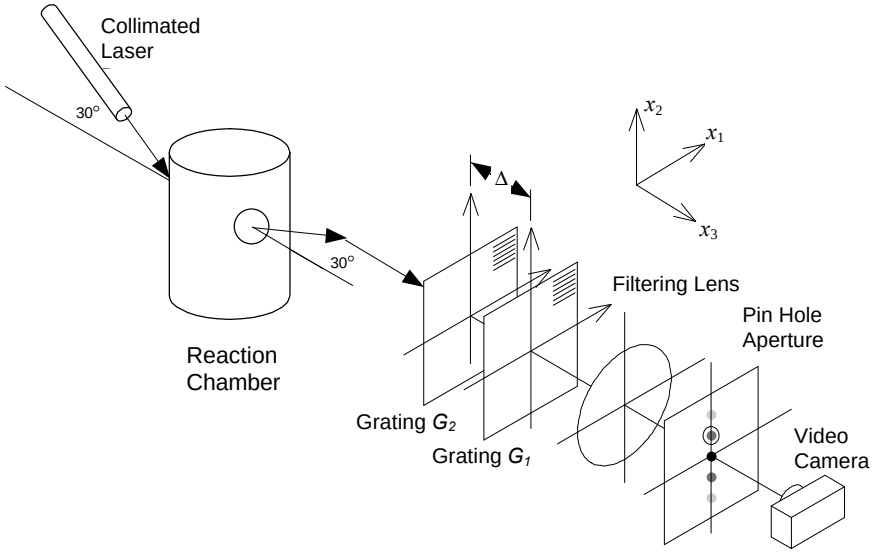

Figure 1: Schematic of the optical beam path for our CGS experimental setup.

and space, optical method developed and first applied to thin films by Rosakis *et al.* [4]. A schematic of the optical path is shown in Figure 1. Initially referenced to a flat surface, a well collimated incident beam is reflected from the sample and passes through a series of two transmission diffraction gratings, which effectively displace or "shear" the beam laterally by a relative amount, ω. The sheared orders are recombined into an image by the filtering lens, and the appropriate order is passed through the aperture to a video camera.

For a given grating of pitch, p, the diffraction angle is given by

$$\theta = \arcsin \frac{\lambda}{p} \ , \tag{1}$$

and the shearing distance is

$$\omega = \Delta \tan \theta \ . \tag{2}$$

For small displacements,

$$\theta \approx \frac{\lambda}{p} \ , \tag{3}$$

and

$$\omega = \Delta \theta \ . \tag{4}$$

The reflected beam arrives at the first of grating with an initial phase of $S\left(x_1, x_2\right)$, as seen in Figure 2, and is split into multiple orders. The first order wavefronts, $\mathrm{E}_{0,1}$ and $\mathrm{E}_{1,0}$, with phases $S\left(x_1, x_2 + \omega\right)$ and $S\left(x_1, x_2\right)$, respectively, are combined to form a "first order" full-field interferogram. For constructive interference, the following conditions must be met

$$S\left(x_1, x_2 + \omega\right) - S\left(x_1, x_2\right) = n^{(2)} \lambda \ , \qquad n^{(2)} = 0, \pm 1, \pm 2, ... \tag{5}$$

Here $n^{(2)}$ corresponds to the observed fringe orders in the x_2 direction. For the reference (optically flat) surface, $n^{(2)} = 0$, the gratings positions are adjusted so that the phase

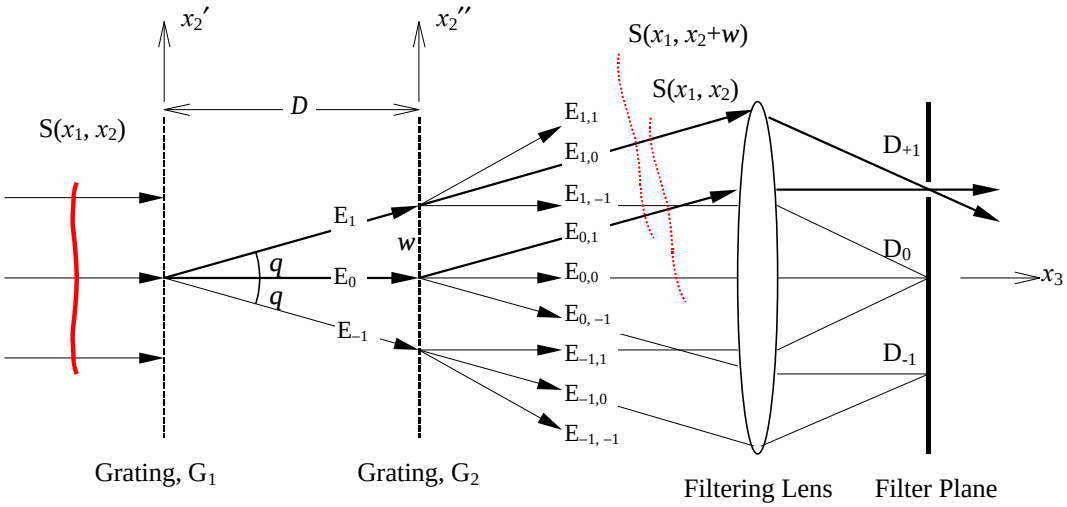

Figure 2: Schematic diagram of the working principle of CGS

difference produces a completely constructive first order interferogram. An additional set of gratings may be added so that the reflected beam may be split and sheared in orthogonal directions to simultaneously obtain the tensor elements. In the limit of $\omega \to 0$,

$$\frac{S\left(x_1, x_2+w\right) - S\left(x_1, x_2\right)}{\omega} = \frac{\partial S}{\partial x_2} = \frac{n^{(2)}\lambda}{\omega} \ . \tag{6}$$

Equation (6) can be rewritten using equation (4) as

$$\frac{\partial S}{\partial x_2} = \frac{n^{(2)}p}{\Delta} \ , \tag{7}$$

and more generally for shearing in the $x_\alpha$direction

$$\frac{\partial S\left(x_1, x_2\right)}{\partial x_\alpha} = \frac{n^{(\alpha)}p}{\Delta} \ , \qquad n^{(\alpha)} = 0, \pm 1, \pm 2, ... \tag{8}$$

To relate the surface curvature to the shearing, consider an incident beam reflecting from a simple surface which can be described as

$$F\left(x_1, x_2, x_3\right) = x_3 - f\left(x_1, x_2\right) = 0 \ . \tag{9}$$

The surface unit normal, $\hat{n}\left(x_1, x_2\right)$ for the curved surface is given as

$$\hat{n} = \frac{\nabla F}{|\nabla F|} = \frac{\hat{\mathbf{e}}_3 - \left(f_1'\hat{\mathbf{e}}_1 + f_2'\hat{\mathbf{e}}_2\right)}{\sqrt{1 + f_1'^2 + f_2'^2}} \ , \tag{10}$$

and the incident and reflected unit wave vectors, $\hat{\mathbf{d}}$ and $\hat{\mathbf{d}}_\mathbf{0}$ (depicted in Figure 3) are given by

$$\hat{\mathbf{d}} = \frac{2\left(-f_1'\hat{\mathbf{e}}_1 - f_2'\hat{\mathbf{e}}_2 + \hat{\mathbf{e}}_3\right)}{1 + f_1'^2 + f_2'^2} - \hat{\mathbf{e}}_3 \ , \tag{11}$$

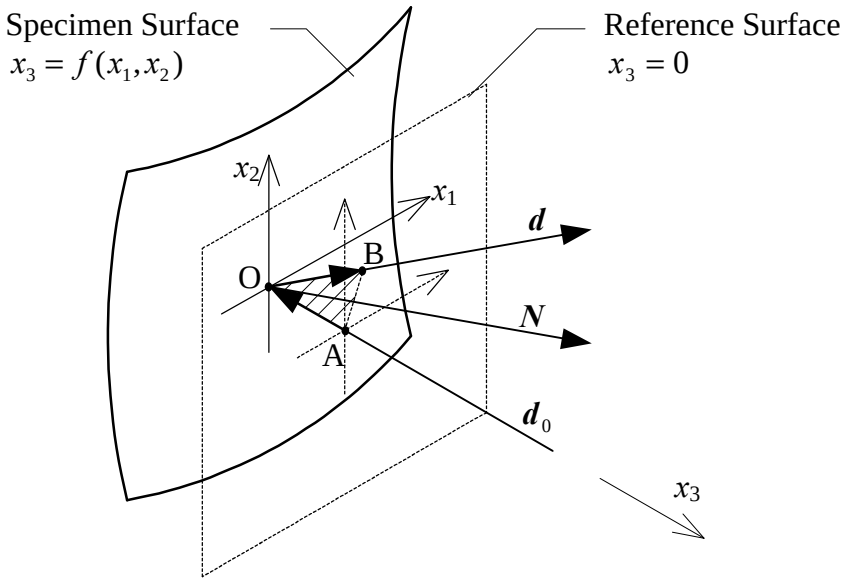

Figure 3: Calculation of the change in path difference relative to a flat reference surface

$$\hat{\mathbf{d}}_0 = -\hat{\mathbf{e}}_3 \ . \tag{12}$$

Compared to a reference surface, $x_3 = 0$, the change in the optical path, $S(x_1, x_2)$, from the specimen surface $x_3 = f(x_1, x_2)$ is given as

$$S(x_1, x_2) = \left|\overrightarrow{AO}\right| + \left|\overrightarrow{BO}\right| = \left|f(x_1, x_2)\,\hat{\mathbf{e}}_3\right| + \left|\left(\frac{f(x_1, x_2)}{\hat{\mathbf{d}}(x_1,x_2)\cdot\hat{\mathbf{e}}_3}\right)\hat{\mathbf{d}}(x_1,x_2)\right| \tag{13}$$

$$S(x_1, x_2) = f(x_1, x_2)\left(\frac{2}{1 - f_1'^2 - f_2'^2}\right) \ . \tag{14}$$

Using equation (8) and the assumption of small curvature such that, $\left|\nabla^2 f\right| \ll 1$,

$$\frac{\partial f(x_1, x_2)}{\partial x_\alpha} \approx \frac{n^{(\alpha)} p}{2\Delta} \ , \qquad n^{(\alpha)} = 0, \pm 1, \pm 2, ... \tag{15}$$

The curvature can be written as

$$\kappa_{\alpha\beta} = \frac{f'_{\alpha\beta}}{1 + f_1'^2 - f_2'^2} \ , \qquad \alpha, \beta \in \{1, 2\} \ , \tag{16}$$

and given once again that $\left|\nabla^2 f\right| \ll 1$,

$$\kappa_{\alpha\beta} \approx f'_{\alpha\beta} \ , \qquad \alpha, \beta \in \{1, 2\} \ . \tag{17}$$

Substitution of equation (15) into equation (17) gives the basic equation that related the observed interferogram fringe density to the curvature tensor.

$$\kappa_{\alpha\beta}(x_1,x_2) \approx \frac{\partial^2 f(x_1 x_2)}{\partial x_\alpha \partial x_\beta} \approx \frac{p}{2\Delta}\left(\frac{\partial n^\alpha(x_1, x_2)}{\partial x_\beta}\right), \qquad n^\alpha = 0, \pm 1, \pm 2, ... \tag{18}$$

which relates the shearing or change in path difference to the observed diffraction orders. In relating the observed fringes to the elements of the curvature tensor, $\kappa_{\alpha\beta}$, it is important to note that any constant displacement $f(x, y)$ has disappeared. This confirms that CGS is insensitive to vibration and rigid body displacement.

EXPERIMENTAL SETUP AND PROCEDURE

We have implemented CGS in our MOCVD reactor to examine the curvature of the film-substrate system throughout the growth and annealing process. For fully grown single-sided films, we have obtained a dynamic map of the magnitude of the average stress under various annealing conditions. The reactor is complicated by a rotating substrate, thermal gradients, and angled viewports.

For fully grown single-sided films, we have obtained a dynamic map of the magnitude of the average stress under various annealing conditions. The experiments were performed in a stainless steel, cylindrical, cold-wall, vertical, stagnation flow reactor [5], where both the sample and its 2.75 inch diameter SiC susceptor rest on an inconel can which houses the resistance heaters. Gas flows vertically through a 3 inch diameter "showerhead" with an array of 313, 1mm holes, 1.5 inches above the sample, and in addition, there is a "shroud" flow of 1.0 s.l.m. of N_2 around the showerhead to contain the flow. A series of mass flow controllers and actuated pumping allows for a constant background pressure to be maintained throughout the runs with flows of O_2 and N_2 ranging from 0 to 5 s.l.m. The flow gas was sampled near the substrate with a mass spectrometer in order to verify the composition of flow near the substrate. Temperature for the initial runs was measured by thermocouple contact to the inside of the can. For the later, fully oxygenated runs, direct thermocouple contact was made with the susceptor.

The optical path through the reactor is at 60° from the sample normal. An 18mWatt HeNe laser is expanded to form a 1.5 inch diameter collimated incident beam. The diffraction gratings have a pitch of 1000 lines/inch, and the grating spacing was 1 inch for the 25 x 25 x 0.5 mm wafer runs and increased to 2 inches for the later runs. The sensitivity of CGS in this arrangement is $0.01\,\mathrm{m}^{-1}$ [6]. Because a single set of gratings was used, curvature in only one direction could be measured during an individual run. The images were captured on a Sony TRV43 camcorder. Although there is some fluctuation of the signal due to thermal gradients, flickering of the signal can be reduced with the strategic use of fans. The images are not affected by flows of up to l0 s.l.m. within the reactor.

The MOCVD YBCO on MgO samples are well oriented, c-axis polycrystalline and were supplied by Superconducting Technologies Inc. [7]. *Ex-situ* CGS measurements of the supplied YBCO-MgO samples reveal them to be slightly curved and spatially non-uniform. The respective curvatures of the bare wafer were not measured prior to production; however, the curvature of the supplied MgO substrates typically have a radius curvature less than $0.01\,\mathrm{m}^{-1}$. XRD results show the presence of strictly 1:2:3 phase YBCO with a typical c-axis length of 11.665Å. Susceptibility measurements indicate a $T_c \geq 80\,^\circ\mathrm{C}$ and $\Delta T_c \sim 1\,^\circ\mathrm{C}$. Reference [7] further details the high quality nature of the supplied samples, and includes AFM images of the samples which show spiral steps characteristic of high quality YBCO films.

RESULTS

To examine the strain due to thermal mismatch between MgO and YBCO, a one inch, square YBCO (700 nm thick) on MgO (0.5 mm thick) sample was heated from room temperature to 760 °C in vacuum in about one hour while simultaneously monitoring the CGS interferograms. The sample was baked *in-situ* at 700 °C for one hour prior to the run to remove excess oxygen; UV reflectance spectra indicate the initial oxygen stoichiometry of the $YBa_2Cu_3O_x$ to be $x \leq 6.3$ [8]. The CGS interferograms for shearing along the x_2 direction are shown in Figure 4.

We use Stoney's equation [9, 10] for thin films, $h_f \ll h_s$,

$$\kappa = 6\varepsilon_f \frac{h_f}{h_s^2} \frac{E_f}{E_s} \frac{(1-\upsilon_s)}{(1-\upsilon_f)} \ , \tag{19}$$

which becomes,

$$\sigma_f = \frac{1}{6} \frac{E_s}{(1-\upsilon_s)} \frac{h_s^2}{h_f} \kappa \tag{20}$$

when written in terms of stress in the film, σ_f. Variables $h_f = 700\,\text{nm}$ and $h_s = 0.5\,\text{mm}$ are the respective film and substrate thickness, $E_f = 148$ GPa [11] and $E_S = 315$ GPa [12] are the respective Young's moduli, $\upsilon_f = 0.255$ [11] and $\upsilon_s = 0.176$ [12] are the respective Poisson's ratios. The measured curvatures from the CGS interferograms are combined with the values presented above and equation (20) to calculate the average stress, σ_f, and strain, ε_f, in each direction. The results are plotted versus temperature in Figure 5, where the strain values are calculated from the following relation,

$$\varepsilon_f = \sigma_f \frac{(1-\upsilon_f)}{E_f} \ . \tag{21}$$

It is important to note that the CGS interferogram alone does not give the sign of the curvature, so the values reported are absolute.

The measured κ_{11} component shows a monotonically increasing stress-strain relationship with increasing temperature, while the measured κ_{22} component indicates similar room temperature values as κ, but exhibits a local minima at 624 °C and then increases to 1.03 GPa above 719 °C.

Exploring the orthorhombic to tetragonal phase transition, we examined fully oxygenated 2 inch diameter wafers from 25 °C to 650 °C under various oxygen conditions. A constant background pressure of 10 torr was maintained throughout the runs with flows of O_2 and N_2 ranging from 0 to 5 s.l.m. The susceptor temperature was cycled between 300 °C and 600 °C in about one hour while monitoring the CGS interferograms. The ratios of O_2/N_2 were 100 : 1 and vice versa for the respective oxygen and nitrogen rich cycles. Figure 6 shows a series of images taken as the temperature is cycled under different oxygen partial pressures. In the N_2 rich cycle (bottom), the initial interferogram remains intact with little change in the magnitude or direction for temperatures up until 558 °C, where we observe a sharp transition in the CGS interferogram in both magnitude and direction. For the O_2 rich cycle (top), we observe a similar transition but at a higher temperature, 584 °C −650 °C. Hence, the transition temperature depends strongly on the O_2 partial pressure. In both cases, the transformation is reversible. By toggling the O_2 and N_2 ratio at 560 °C, the interferogram was seen to revert repeatably from an oxygenated state to a deoxygenated state and back.

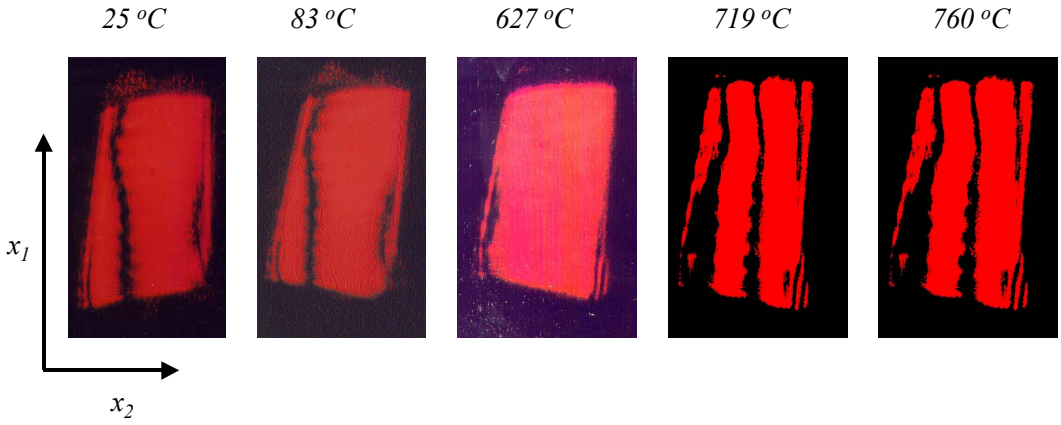

Figure 4: Series of CGS interferograms of YBCO on MgO with increasing temperature (left to right). Shearing is along the x_2 direction (κ_{22}).

We find the curvature to be higher for oxygen rich conditions over the temperature range studied. Figure 7 shows CGS interferograms of a similarly prepared YBCO-MgO wafer held at constant temperature, 615 °C (±10 °C), with O_2 and N_2 flows. The total pressure is 100 torr. With the higher pressure, we see that the curvature doubles within about 7 minutes of changing the flow. Figure 6 illustrates this behavior.

CGS analysis was also implemented during YBCO film growth. Figure 8 shows three images of a 2 in substrate during the MOCVD growth of YBCO. Notice that despite film deposition, the basic fringe pattern does not change. This growth, resulted in a 365 nm thick film with nearly perfect 1:2:3 stoichiometry, begins and ends (after 2 hours) with the fringe count of 5.8 as depicted in the figure. CGS analysis of several growth runs confirms that there is no change in curvature as YBCO films are deposited in our MOCVD reactor (the notable caveat is that no films have been grown to thicknesses > 500 nm with *in-situ* CGS analysis).

Figure 8 is also interesting because the initial substrate had a structural defect in the single crystal of MgO. In the first interferogram (uncoated MgO), there is a fingerprint type of fringe pattern in the upper right of the interferogram. This fingerprint pattern indicates local stresses around the defect. As the YBCO is deposited, the defect is covered up by a smooth film of YBCO, and the associated fingerprint pattern eventually vanishes.

DISCUSSION

For the non-stoichiometric case, our stress-strain values from the measured κ_{11} and κ_{22} components are 0.4 and 0.6 GPa respectively. As seen in Figure 5, at room temperature, the stress values derived from κ_{11} and κ_{22} are similar, but there is a dramatic decrease in the κ_{22} component near 624 °C which is indicative of a phase transition.

From published values [3] for varying thickness of YBCO films on MgO (0.5 mm thick x 10 mm diameter) grown by spray pyrolysis at 900 °C, we estimate the average stress produced from a 700 nm film to be -0.7GPa at room temperature. The average stress values were obtained at room temperature from a series of bending tests, which showed the stress to be concentrated at the center of the sample. The stress is attributed to the lattice mismatch

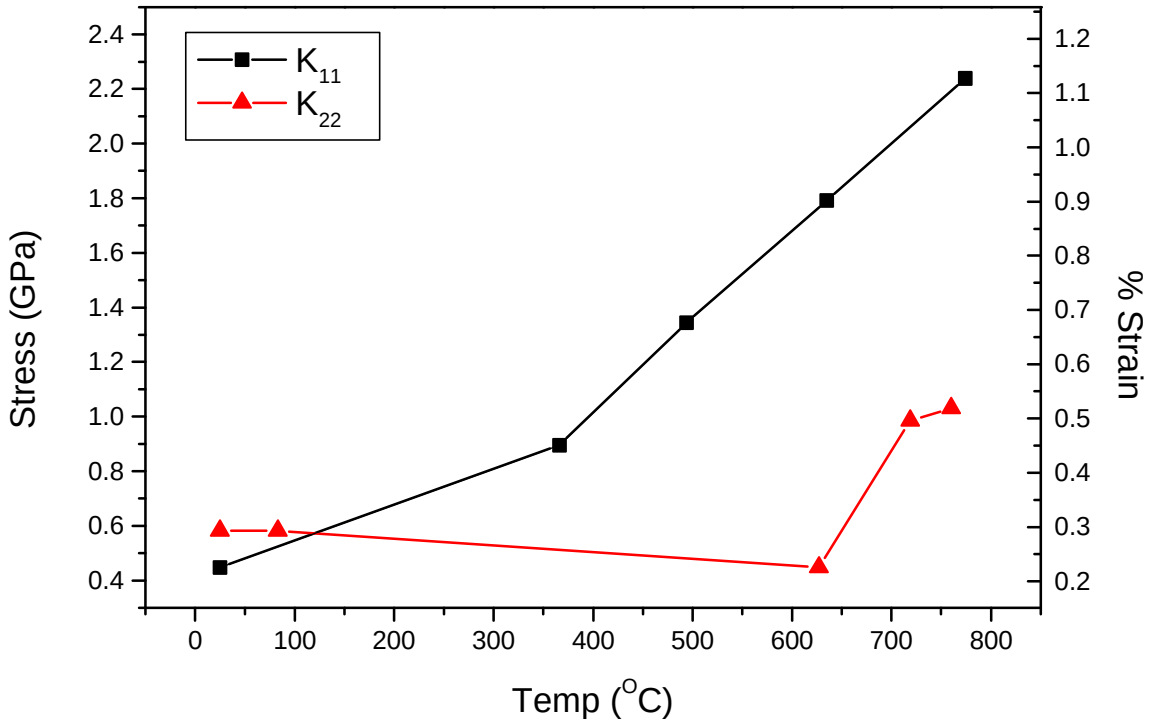

Figure 5: Stress and strain values calculated from the CGS interferograms presented in Figure 1.

between YBCO and MgO, although the films are not completely stoichiometric and show a substantial amount of Y_2BaCuO_5 at the substrate-film interface. SEM images of the samples do not reveal characteristic spirals found in well oriented, c-axis films. Nonetheless, the values of stress computed for our films compare well with the literature.

Of particular interest are the changes in the curvature components with temperature. Stress due to thermal mismatch can be computed using the following relation,

$$\sigma_f = \frac{\Delta T\,|\alpha_f - \alpha_s|}{\alpha_s \Delta T + 1} \frac{E_f}{1 - \upsilon_f}\ , \tag{22}$$

where α_f and α_s are the respective coefficients of linear expansion [13]. Although values for MgO over a broad temperature range are well known ($\alpha_{MgO} = 14 \times 10^{-6}\,\mathrm{K}^{-1}$ at 900 K [14]), similar properties for YBCO are not. For a temperature difference of $\Delta T = 750\,^{\circ}\mathrm{C}$, the coefficient of linear expansion is $21.6 \times 10^{-6}\,\mathrm{K}^{-1} < \alpha_f < 28.9 \times 10^{-6}\,\mathrm{K}^{-1}$ which is high compared to results for YBCO (4000 nm) on MgO buffered $SrTi0_3$ substrates, $\alpha_{YBCO} = 13.4 \times 10^{-6}\ \mathrm{K}^{-1}$ [13]. Even the theoretical maximum coefficient of thermal expansion for YBCO single crystal material in the (100) direction is only $23 \times 10^{-6}\,\mathrm{K}^{-1}$ [15]. As a result, we cannot explain the observed curvature entirely by thermal mismatch [1, 16].

Strain effects due to phase transitions are of great interest [17]. For stoichiometric YBCO, we compare our results to published phase diagrams [18]. Although the data for thin film YBCO is limited, it is clear that for bulk samples between 400 °C and 700 °C, YBCO undergoes an orthorhombic to tetragonal phase transition and that the transition temperature is proportional to the O_2 partial pressure, which is in agreement with our results. It is not clear from how the macroscopic curvature is affected by such a transition. For polycrystalline

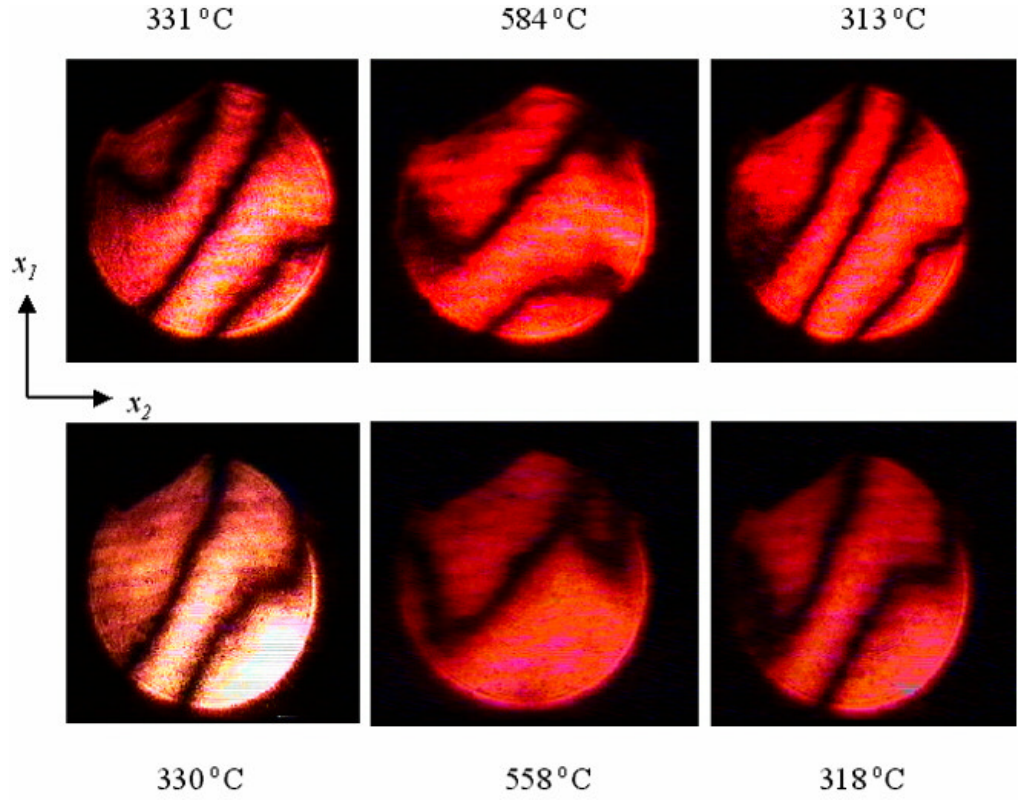

Figure 6: Series of CGS interferograms of YBCO on MgO with showerhead flows of 5.0 s.l.m of O_2 (top) and N_2 (bottom). Total pressure is 10 torr. Shearing is along the x_1 direction.

YBCO with the c-axis normal to the plane but with misaligned grains, there could be an averaging of the a and b axis to give a slightly larger effective lattice spacing such that the κ_{11} and κ_{22} change somewhat equally. However, if the grains are well aligned, twinning could produce a non-uniform change in curvature. Also, film thickness and coverage certainly have an effect on the macroscopic stress exhibited by a film substrate system, for this reason we do not believe that the CGS images are unique to this particular phase transition, however we do expect a relaxation upon the phase change. Although not fully understood, the observed increase in stress with increase oxygen flow in Figure 7 could be related to a non-equilibrium phase state of the YBCO.

In order to further understand the effect of oxygen on the macroscopic curvature, it will be necessary to monitor the oxygen content, *in-situ,* which is possible with UV reflectance. For YBCO, an observable phase transition could be very useful in the annealing process to determine the final oxygen concentration, since current YBCO production consists of *ex-situ* oxygen annealing for several days. (Typically the oxygen stoichiometry is determined from weighing and or from X-ray diffraction.)

CONCLUSIONS

CGS holds promise as a diagnostic technique: it provides a simple, full field, intuitive image of the curvature tensor under a wide range of run conditions. For thin film YBCO on MgO, we are able to observe changes in the macroscopic curvature of a sample due to

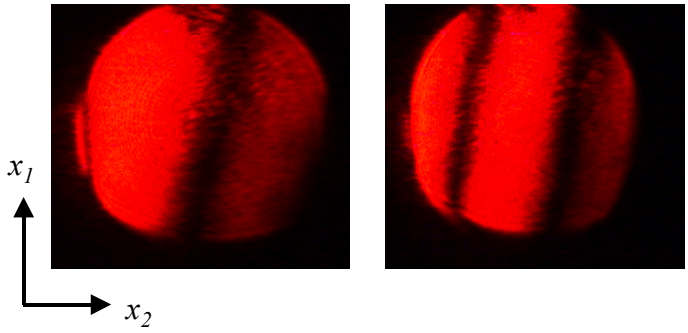

Figure 7: CGS interferograms of YBCO on MgO at 615 °C (±10 °C) under O_2 (right) and N_2 (left) flows of 5.0 s.l.m. Total pressure is 100 torr. Shearing is along the x_1 direction.

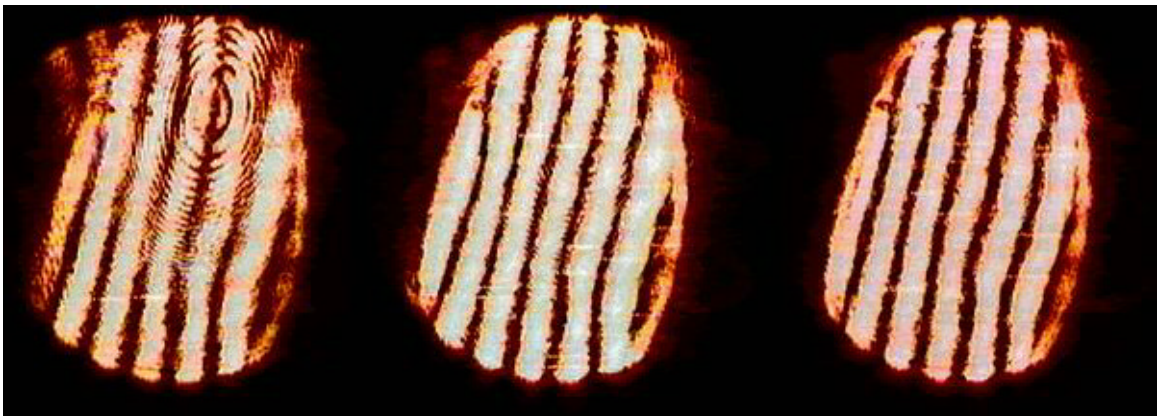

Figure 8: CGS interferograms of YBCO growth on MgO. From left to right, the elapsed growth time is , 0 min, 8 min, and 29 min.

thermal mismatch and phase transition under run conditions. For YBCO, we find the curvature to be a strong function of the oxygen stoichiometry and sample temperature. Conversely, growth of YBCO on MgO does not exhibit any changes in curvature, indicating that the growth process occurs in equilibrium. Further, with simple modifications to the standard arrangement, we hope to deduce the full tensor and the sign of the each of the tensor components.

ACKNOWLEDGMENTS

This work was supported by DARPA/NSF DMS-9615858. The authors would like to thank Martha Gallivan, Jurgen Musolf, Rob Kukta, and Kaushik Bhattacharya for their helpful contributions.

References

[1] S. Auzary, K.F. Badawi, L. Bimbault, J. Rabier, R.J. Gaboriaud, and P. Goudeau. J PHYS III 7: (1) 35-46 JAN 1997.

[2] S. Auzary, F. Badaw, L. Bimbault, J. Rabier, and R.J. Gaboriaud, J of Alloys and Compds. **251** (1997) 37-4.

[3] W. Wu, M.T. Lanagan, M.L. Jullberg, R.B. Poeppel, B. Wang, and S. Danyluk, Thin Solid Films, **223** (1993) 260-268.

[4] A.J. Rosakis, R.P. Singh, Y. Tsuji, E. Kolawa, and N.R. Moore Jr., Thin Solid Films, **325**, 42 (1998).

[5] A.B. Tripathi, D.A. Boyd, M.A. Gallivan, R.M. Murray, H.A. Atwater, D.G. Goodwin, L.R. Raja, R.J. Kee, and J. Musolf, "A Stagnation-Flow MOCVD Reactor For Intelligent Deposition of YBCO Thin Films.", in Proceedings of the Electrochemical Society Spring Meeting (2000)

[6] H. A. Bruck and A. J. Rosakis, Optics and Lasers in Engineering **18** (1993) 25-51.

[7] J. Musolf and E. Smith IEEE T APPL SUPERCON 9: (2) 2167-2170 Part 2 JUN 1999.

[8] J. Kircher, M.K. Kelly, S. Rashkeev, M. Alouani, D. Fuchs, M. Cardona, PRB **44**, 1 (1991) 217-224.

[9] G.G. Soney, Proceedings of the Royal Society, London, Series A, **82**, 172 (1909).

[10] L.B. Freund, J.A. Floro, E. Chason, APL 74 (1999) 1987-1989.

[11] H. Ledbetter and L. Ming, J. Mater. Res., **6**, 2253 (1991)

[12] G. Simmons and H. Wang, *Single Crystal Elastic Constants and Calculated Aggregate Properties: A Handbook*, MIT Press, Cambridge (1971)

[13] J. Kawashima, Y. Yamada, Hirabayashi I, PHYSICA C 306: (1-2) 114-118 SEP 10 1998.

[14] J. Shanker, S.S. Kushwah, and P. Kumar, Physica B, **78**, 223 (1997)

[15] J.D. Jorgensen, M.A. Beno, D.G. Hinks, L. Soderholm, K.J. Volin, R.L. Hitterman, J.D. Grace, I.K. Schuller, C.V. Serge, K. Zhang, and M.S. Kleefisch, Phys. Rev. B, **36**, 3608 (1987)

[16] J. Maeda , Y. Nakamura, T. Izumi, Y. Shiohara, SUPERCOND SCI TECH 12: (8) 563-565 AUG 1999.

[17] A. M. Bratkovsky, V. Heine, E.K.H. Salje PHILOS T ROY SOC A 354: (1720) 2875-2896 DEC 15 1996.

[18] T.A. Vanerah, R.S. Roth, H.F. McMurdie, eds *Phase Diagrams for High Tc Superconductors II,* Westerville, Ohio : American Ceramic Society, c1997.